The Effects of Toolpath and Glass Fiber Reinforcement on Bond Strength and

Dimensional Accuracy in Material Extrusion of a Hot Melt Adhesive

Masoumeh Pourali and Amy M. Peterson*

University of Massachusetts Lowell, Department of Plastics Engineering, Lowell, MA, United States

*Corresponding Author

Email Address: Amy Peterson@uml.edu

Abstract

In this work, a polyamide hot melt adhesive (Technomelt PA 6910) and its glass fiber-filled

composite (Loctite 3D 6910) were evaluated as feedstocks for desktop-scale thermally-driven

material extrusion additive manufacturing (AM). Technomelt PA 6910 is a semicrystalline

polymer with a sub-ambient glass transition temperature, intermediate melting temperature,

and low recrystallization temperature. This paper aims to study the effect of glass fibers and

toolpath on mechanical properties, warpage, and dimensional accuracy of prints. Glass fibers

improved the yield strength of 0° raster angle bars, but reduced the strength of 90° raster angle

samples. The reduced weld strength was more significant in samples cut from single road width

boxes than multilayer (≈3.2 mm thick) specimens due to fast cooling of thin parts. Glass fibers

prevented warpage and excessive spread of initial layers of boxes. Toolpath affected tensile

properties for Technomelt PA 6910, in which longer toolpaths resulted in higher warpage and

decreased tensile strength of parts due to longer layer times, but did not affect tensile properties

for Loctite 3D 6910. While Technomelt PA 6910 exhibits isotropic tensile properties, the addition

of glass fibers resulted in anisotropic properties of Loctite 3D 6910 bars, which was more

significant in single road (≈0.4 mm thick) parts. Multilayer Loctite 3D 6910 structures are

stronger, which makes this material more appropriate for larger scale applications in which there is a high thermal mass and slumping is a big printing challenge.

Keywords: Additive manufacturing; Material Extrusion; Tool path; Glass fibers; Warpage

1. Introduction

Fused filament fabrication (FFF) is a thermally-driven form of material extrusion additive manufacturing (MatEx). FFF, which is the most common additive manufacturing (AM) technique for thermoplastics, uses thermoplastic filaments as feedstocks that are heated until molten and then deposited on a print bed layer-by-layer. Broader adoption of FFF is limited by poor adhesion between layers, anisotropic mechanical properties of prints, and build-up of residual stresses within the parts [1–4]. Fast cooling and heating of layers in FFF result in complex crystallization behavior in semicrystalline polymers [5], and substantial thermal gradients between the layers, which cause residual stresses within the parts [6–8]. In semicrystalline polymers, the highly ordered and packed polymer chains of the crystalline domains shrink more than the amorphous phases, which results in larger thermomechanical stresses and warpage of prints [9–12]. Therefore, despite the good toughness, chemical resistance, and thermal resistance that semicrystalline polymers offer, amorphous polymer or semicrystalline polymers that do not crystalline substantially during FFF are far more commonly used in FFF.

Controlling the temperature of the printing chamber [13–15], increasing temperature of the deposited layer before deposition of the next layer [16–18], using fillers to decrease the coefficient of thermal expansion (CTE) [19–21], and increasing thermal conductivity of the

polymer through conductive fillers [21] are some of the approaches that have been investigated to control warpage and mechanical properties of FFF prints. These approaches suppress print warpage by reducing the thermal gradient, reducing the volume of warpage-prone polymer, and/or increasing part stiffness. Heating the build plate, applying a thin layer of adhesives, and selecting the appropriate build plate material are other common approaches to avoid part delamination from the build plate during printing [22–24]. For example, Schirmeister et al. successfully printed highly crystalline HDPE by using poly(styrene-block-ethene-co-butene-block-styrene) thermoplastic elastomer (SEBS) as the build plate material, which prevented part delamination from the build plate [22].

Compounding semicrystalline polymers with fillers or blending them with amorphous polymers are common approaches used for controlling the crystallization rate and warpage of prints [25–27]. Fillers can reduce warpage by decreasing the coefficient of thermal expansion and also by increasing the thermal conductivity of the composite, which depends on the filler type and loading [19–21]. Fillers can also provide improved mechanical properties of prints in the desired direction [19,28]. For example, Sodeifian et al. found that the addition of short glass fibers in polypropylene (PP) improved the strength and modulus of prints and reduced their warpage [27]. Tekinalp et al. has shown that the tensile strength and tensile modulus of ABS parts can be improved by compounding with up to 20% and 30% carbon fibers, respectively. However, adding more carbon fibers resulted in a significant increase in internal voids inside the beads due to the weak adhesion between fibers and the matrix, which resulted in deteriorated mechanical properties of prints [29]. In another study by Gupta et al., compounding polycarbonate (PC) with short carbon fibers could not suppress warpage completely, and a closed chamber with a

controlled temperature of 50 °C was used to prevent the warpage and delamination of prints from the build plate. The printed composite parts exhibited slightly lower tensile strengths as compared to the printed neat polymer, which is related to the formation of local stresses produced by the imperfect alignment of short fibers [30]. These results highlight that certain requirements need to be fulfilled for fiber-reinforced composites to ensure consistent properties throughout the printed part, such as good adhesion between the fiber and matrix, homogeneous distribution of fibers in the matrix, strong interlayer bonding, and low porosity [31].

In this study, FFF structures made with Technomelt PA 6910 and Loctite 3D 6910 (glass fiber-filled Technomelt PA 6910) are compared in terms of their mechanical properties, dimensional accuracy, and warpage. Technomelt PA 6910 is a polyamide-based hot melt adhesive based on a proprietary blend of diacids and diamines. FFF of Technomelt in our previous study resulted in void-free parts with isotropic mechanical properties [32], while Loctite was used for building 8 m² urban cabins in Amsterdam with large-scale MatEx [33], which make these materials interesting for further study. Single road boxes with different wall lengths were printed to allow for the investigation of the effect of toolpath length on print properties and provide a simple model for subsequent thermal modeling.

2. Materials and Methods

2.1 Materials

Technomelt PA 6910 and Loctite 3D 6910 were kindly provided by Henkel Corporation in the form of strand cut pellets. Technomelt PA 6910 is a semicrystalline polyamide-based hot melt adhesives based on a proprietary blend of dimer fatty acids and diamines. Loctite 3D 6910 is

essentially a glass fiber-filled Technomelt PA 6910. Loctite 3D 6910 contains 12.5±0.2 wt% glass fiber based on thermogravimetric analysis (TGA), which is discussed later. For the rest of the paper Technomelt PA 6910 and Loctite 3D 6910 will be referred as Technomelt and Loctite, respectively.

2.2 Filament Extrusion

A Dr. Collin single screw extruder (COLLIN Lab & Pilot Solutions GmbH) was used to extrude Technomelt filaments with a diameter of 2.85±0.06 mm and Loctite filaments with a diameter of 2.85±0.04 mm using a 3.5 mm diameter die. The transition zone of the extruder was set to a melting temperature of 195 °C for Technomelt and 210 °C for Loctite. A screw speed of 20 rpm was used for both materials. The extruded filament was water cooled and a Davis-Standard Corporation caterpillar puller was used to adjust the filament diameter by pulling at a speed of 19.8 rpm for Technomelt and 21 rpm for Loctite. A tight tolerance in filament diameter is critical for achieving uniform material extrusion during FFF. Therefore, filament diameter was measured using a digital caliper every 30 seconds during extrusion to assure a tight tolerance along the whole length of the collected spools of filament.

2.3 FFF

Single wall hollow boxes of Technomelt were printed on an Ultimaker 3, while single wall hollow boxes of Loctite were printed on a Lulzbot TAZ6. Attempts to print Loctite on the Ultimaker 3 printer were unsuccessful due to nozzle clogging and filament grinding. Ultimaker offers multiple print cores for their extruders. The Ultimaker 3 AA print core has a step transition to reduce oozing, but this shape creates a dead zone during material extrusion that leads to

nozzle clogging when printing with this fiber-reinforced material. The BB print core provides a smooth path for the material to flow to prevent nozzle clogging. However, under-extrusion was a common problem due to backflow [4] of the material and filament grinding in the pulling gears of the printer. Therefore, Loctite was printed on a Lulzbot TAZ6 with a direct feeding system and a similar nozzle geometry to the Ultimaker BB print core. The TAZ6 could not be used for printing Technomelt because of filament buckling in the free distance between the pulling gear and the print core. Cura 4.3 and Cura Lulzbot 3.6.8, which are both open-source slicers, were used to generate G-code for the Ultimaker 3 and Lulzbot TAZ6, respectively.

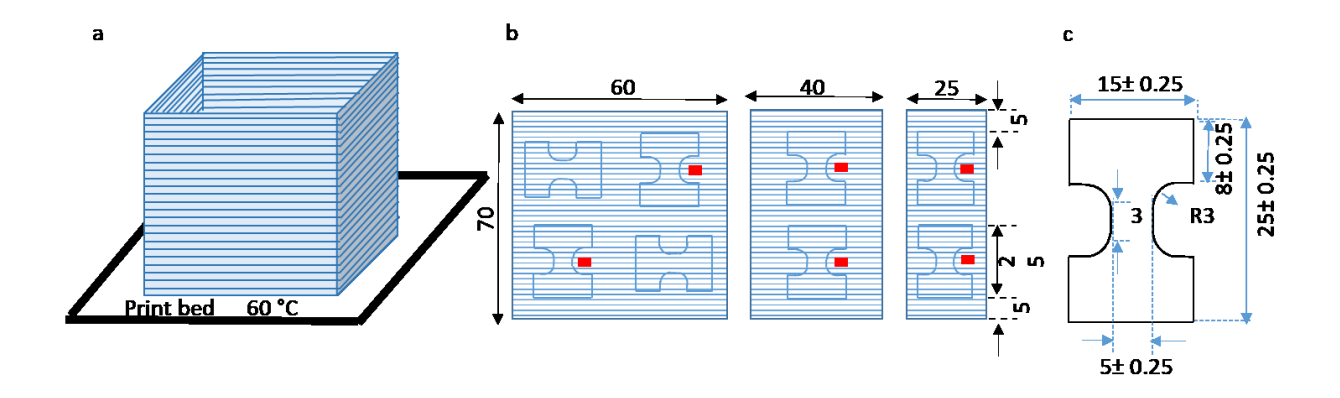


Figure 1. Schematic of: a. Printed boxes; b. Laser cut plan for cutting micro tensile bars from walls of the boxes; c. Dimensions of tensile bars. Dimensions of walls and tensile bars are in mm.

The extruder temperature was set to 220 °C for Technomelt and 240 °C for Loctite. A print speed of 10 mm/s, layer height of 0.15 mm, and build plate temperature of 60 °C was used for both materials. Boxes were printed with three different wall lengths (25 mm, 40 mm, and 60 mm) as shown in Fig. 1 to study the effect of toolpath on mechanical properties of prints. Type V tensile bars of Loctite were also designed in accordance with ASTM D638-14. The dimensions are specified in Fig. SI 1. The type V samples' print path included a single road wall around the perimeter, with printing parameters similar to those of boxes, except a print speed of 30 mm/s

and infill of 110 % were used. Six samples were tested per condition. A lower printing speed was used when printing boxes to avoid defects due to the increased vibration as a result of increased printing speed. Type V Loctite bars were printed at 30 mm/s, which was the highest print speed that could be achieved without filament buckling in the printer's feeding system. This print speed was the same as that used for Technomelt printing in our previous work [32].

2.4 Thermal Analysis

Thermal analysis was used to determine transition temperatures and to investigate the effect of toolpath on crystallization across print layers. TGA was performed on as-received pellets of Loctite to determine the degradation temperature and weight percent of glass fibers within the Loctite using a Discovery TGA (TA Instruments, New Castle, Delaware). The samples were heated at 20 K/min to 700 °C under a nitrogen atmosphere. A representative graph from TGA results is shown in Fig. SI2, and the percent glass fibers in Loctite is calculated to be 12.5±0.2 wt% based on three replicates of TGA. The SEM image from the fractured cross-section of a Loctite filament in Fig. SI3 shows very high levels of fiber orientation in the extrusion direction.

Differential scanning calorimetry (DSC) was performed at the same layers as the gauge length of the tensile bars, as shown by red rectangles in Fig. 1. DSC was conducted on three samples for each case using a Discovery DSC (TA Instruments). The samples for DSC were prepared in aluminum hermetic pans. Samples were heated from -30 °C to 150 °C at a heating rate of 10 K/min.

2.5 Tensile Testing

Ten micro tensile bars were cut from the walls of boxes for each condition by laser cutting. The laser cutting parameters were selected to reduce the thickness of the heat affected zone (HAZ) and prevent impact on the properties of prints. The dimensions of the specimens were modified from the test specimen defined in ASTM D1708 in a manner previously described by Coogan and Kazmer [34]. The tensile bars were cut from the walls using a 60 W Epilog Legend 36EXT laser cutter according to the cutting plan illustrated in Fig. 1. Vertical (90° raster angle) specimens were cut from all boxes to study the bond strength between layers, and horizontal (0° raster angle) specimens were cut from boxes with a wall length of 60 mm to test the longitudinal strength. Specimens for all conditions were collected from the top and bottom of boxes to study the effect of wall location on mechanical properties. Tensile testing of micro tensile bars was conducted on an Instron 4444 with a 2 kN load cell in accordance with ASTM D1708. Testing speeds of 1 mm/min and 10 mm/min were used for Loctite and Technomelt, respectively. The chosen speeds resulted in similar rates of strain as testing using ASTM D638, which is a condition of ASTM D1708. The reported yield strength and tensile strength values are based on the bonded area of bars for 90° specimen. Bonded area is defined as the product of a bar's measured gage width and the measured bond width between layers as determined using ImageJ as an image processing tool. For 0° specimens, cross-sectional areas are calculated using ImageJ and the tensile properties are normalized to the calculated values.

Tensile testing of type V bars was conducted on an Instron 4444 with a 2 kN load cell in accordance with ASTM D638. The testing speeds for type V samples were chosen as 10 mm/min for Loctite in order to avoid rupture times less than 30 seconds and higher than 5 minutes as is recommended in ASTM D638.

Since different testing speeds were used, qualitative comparisons across conditions are appropriate.

2.6 Optical Microscopy (OM)

OM was performed with a DMi 1 microscope (Leica Microsystems) on cryogenically fractured cross-sections of Technomelt boxes to study the road dimensions from boxes with different wall lengths.

2.7 Scanning Electron Microscopy (SEM)

SEM was performed with a JEOL JSM 6390 (Jeol USA Inc) on cryogenically fractured cross-sections of Loctite boxes with different wall lengths to investigate the effect of layer time on road width of printed layers. SEM was also performed on tensile fractured and cryogenically fractured cross-section of type V Loctite bars to investigate fiber orientation and to determine fracture types in 0° and 90° samples.

2.8 Rheology

Rheological characterization was conducted using capillary rheology on as-received pellets at temperatures from 140 °C to 240 °C in 20 °C increments to determine the viscosity of Loctite and Technomelt at shear rates ranging from 1000 1/s to 7000 1/s. Capillary rheology was conducted using a Dynisco LCR 7000 rheometer (Franklin, Massachusetts).

2.9 Warpage Analysis

Warpage analysis was performed on cryogenically fractured cross-sections of Technomelt boxes.

The amount of warpage was measured based on the deformation of the walls from the designed fully vertical geometry using Image J software.

3. Results and Discussion

3.1 Micro Tensile Bars

The tensile properties of micro tensile bars cut from Technomelt and Loctite boxes according to Fig. 1 are shown in Fig. 2. Yield strength (σ_v) values of all Technomelt specimens are in the same range, regardless of the raster angle, the box height from which the tensile bar was taken, or box wall length. The 0° Technomelt bars exhibit 5% higher average yield strength than all other conditions, and the difference is statistically significant at a 95% confidence interval (one-way analysis of variance, p < 0.05). This difference is sufficiently small that it could be accounted for through load cell drift. Therefore, while the difference in yield strength between 0° Technomelt bars and other conditions is statistically significant, we do not think that it is due to differences in the physical structures of the tested samples. Isotropic tensile properties of Type V Technomelt tensile bars are reported in our previous work [32], so yield strengths independent from the tested variables would be consistent with the superior mechanical properties previously observed in this material.

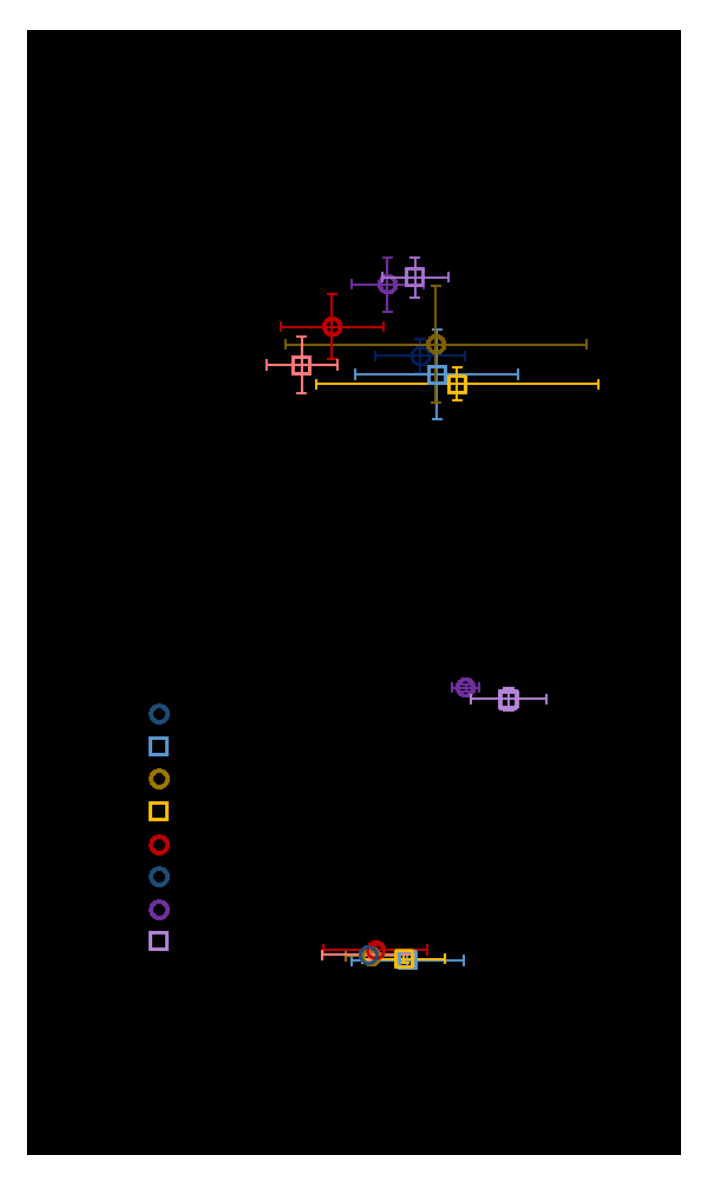


Figure 2. Yield strength versus yield strain for specimens cut from boxes of: a. Technomelt; b. Loctite. Samples are named according to the wall length, the location from where the tensile bar was cut (B = bottom, T = top), and the orientation of printed roads with respect to the loading direction. Error bars represent 95% confidence intervals.

Loctite micro tensile bars with a raster angle of 0° yield at significantly higher stresses than 90° samples, which is expected for FFF prints. Additionally, fiber alignment in fiber-reinforced FFF structures occurs in the direction of the printed roads [29,36]. Loctite specimens with a raster angle of 90° exhibit similar σ_y values with no statistically significant difference, regardless of box wall length or the box height from which the tensile bar was taken.

In comparing Fig. 2a and Fig. 2b, the yield strength of Technomelt micro tensile bars with a raster angle of 90° is approximately 1.5 times higher than the yield strength of Loctite counterparts, which implies worse welding of Loctite bars. However, the 0° Loctite bars exhibit slightly higher yield strength than 0° Technomelt bars due to the reinforcing effect of fibers and negligible effect of weld strength on tensile properties.

The tensile strength (σ_f) vs break strain (ϵ_f) of micro tensile bars for Technomelt and Loctite are plotted in Fig. 3a and Fig. 3b, respectively. Among Technomelt specimens, 0° tensile bars are the strongest due to the orientation of roads parallel to the pulling direction. The intermediate strength group includes the bars from 25 mm boxes and bottom bars from 40 mm boxes. The top bars from 40 mm boxes and the 90° specimens from 60mm boxes comprise the weakest group. Among the Loctite specimens, the 0° specimens are the strongest group, while 90° samples for all box sizes show similar strength with an immediate break after yielding as shown in the representative stress-strain curve in Fig. 4. The large gap between tensile strength of 0° and 90° Loctite bars indicates weak interlayer bonding. Despite the higher yield strength of 0° Loctite bars, their tensile strength is lower than that of Technomelt counterparts, which is due to the embrittlement effect of fibers. Fibers improve the stiffness of the composite and result in minimal plastic deformation of the tensile bars before failure [37]. This is very different from the strain hardening observed in Technomelt bars, which is characteristic of ductile materials [38]. The decreased failure strain of 90° Loctite bars compared to 90° Technomelt counterparts is due to the poor welding between layers and the rigidity of the material caused by glass fibers. Glass fibers reduce the wettability of layers and restrict polymer diffusion in the weld zone, which cause fracture right after yielding with no plastic deformation.

Welding between FFF roads can be explained by the healing model proposed by Wool et al. [39,40]. Healing occurs over five steps: surface rearrangement, surface approach, wetting, diffusion, and randomization. Wetting and diffusion of polymer chains at the welding interface control the ultimate strength of weld, both of which are faster at higher temperatures [35]. The other contributing factor for the weld strength of semicrystalline polymers is crystallization during solidification. Initiation of crystallization before proper diffusion can result in lower chain mobility and limited diffusion of chains in the weld interface. However, growth of crystallites across the interface result in improved interlayer properties [41–43].

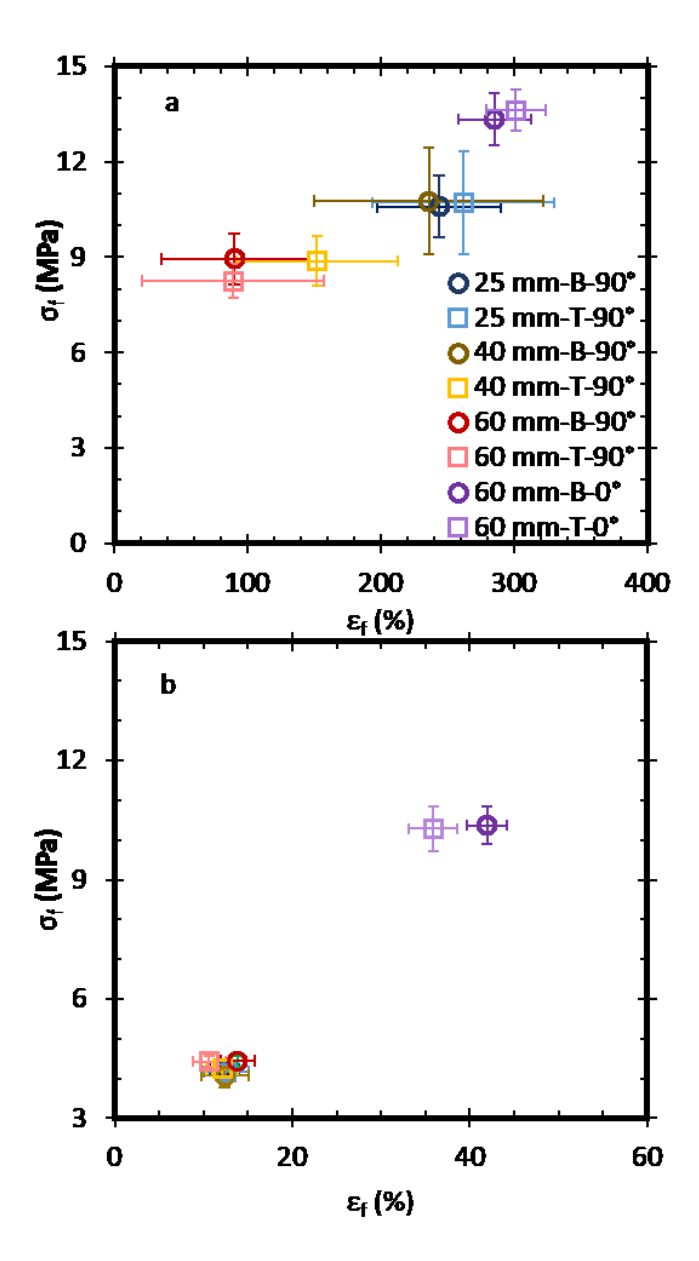


Figure 3. Tensile strength versus strain to failure of the tensile bars cut from boxes of: a. Technomelt; b. Loctite. The legend includes the wall length, the location from where the tensile bar was cut, with B indicating bottom and T indicated top, and the orientation of printed roads with respect to the loading direction. The tensile strength is normalized to the bonding area. Error bars represent 95% confidence intervals.

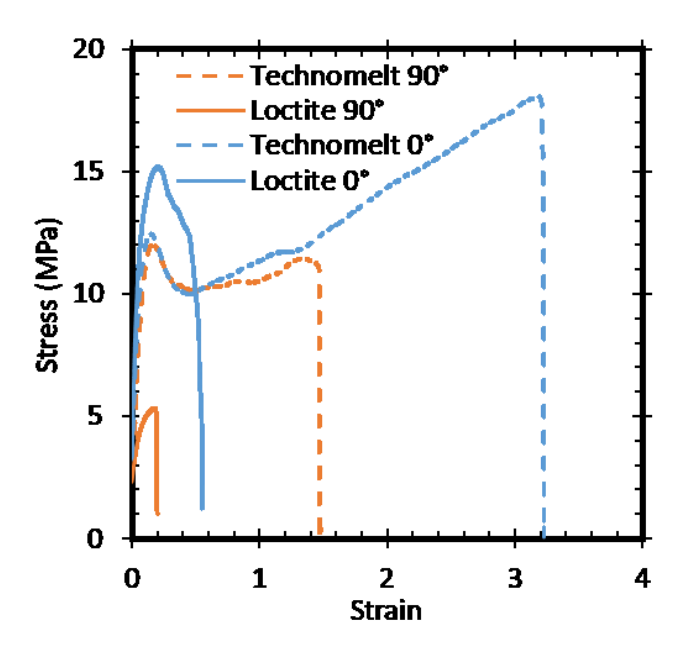


Figure 4. Representative tensile testing results of laser cut micro tensile bars from bottom of 60 mm boxes of Technomelt and Loctite with either 0° or 90° raster angle. A larger version of this figure as well as a separate figure that only includes strains up to 100% is shown in Fig. SI4.

3.2 DSC analysis

Fig. 5 shows results from DSC analysis of samples from the top and bottom of boxes within the gauge length as shown by red rectangles in Fig. 1. There is no significant difference in the amount of crystallinity in the top and bottom tensile bars or at different box wall lengths, which is consistent with the similar values of σ_{V} and indicates that the percent crystallinity is not a contributing factor to differences in tensile strength. We previously reported a melting enthalpy of 23.44±0.7 J/g for type V Technomelt bars [32], which is similar to the melting enthalpy of 24.47±2.2 J/g for printed boxes in this study; however, the relative peak sizes differ greatly as shown in Fig. SI5. Double melting peaks are observed in DSC analysis of boxes indicating two distinct crystalline morphologies. The first melting peak is attributed to an unstable γ -phase and the second melting peak is attributed to a more stable α -phase [44]. The fast cooling in single wall boxes results in lower annealing times and formation of unstable crystallites. However, in type V

tensile bars the unstable γ -phases are replaced with more stable α crystallites, and the high temperature melting peak becomes more dominant. More stable crystallites in type V tensile bars may contribute to their higher weld strength.

We previously studied crystallization of Technomelt and found that its crystallization kinetics are slow and result in one-dimensional crystal growth [44]. Slow crystallization of crystallites allows enough time for complete welding between layers, and the small size of crystallites reduces the negative impact of crystallites on chain mobility and diffusion, which results in isotropic tensile properties of Technomelt prints. On the other hand, crystallization is an exothermic process, which is accompanied by heat release. The released heat during crystallization can improve bond strength of printed parts by delaying the cooling of layers [45].

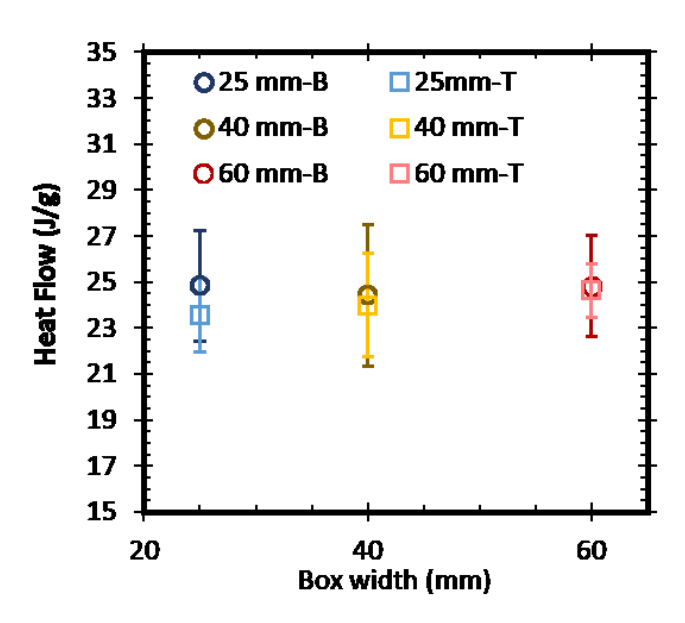


Figure 5. Melting enthalpy results from DSC of Technomelt from the gauge length of tensile bars cut from top and bottom of printed boxes with different lengths. Error bars represent 95% confidence intervals

3.3 Warpage Analysis

Warpage analysis was performed on the cross-section of box walls with different lengths as shown in Fig. 6. Strong adhesion between the print bed and the first layer of prints prevents delamination of the part from the print bed, and warpage is observed as severe plastic deformation in box walls.

Warpage was measured for 40 mm and 60 mm boxes in three regions along box walls, where the warpage has changed its direction and was at its maximum level. From Fig. 6c and 6d, the first warpage presents as an outward bulge at the bottom of the boxes, followed by an inward bulge in the middle, and then an outward bulge at the top of the wall. The maximum amount of warpage in these three regions and their location from the bottom of the boxes are plotted in Fig. 7.

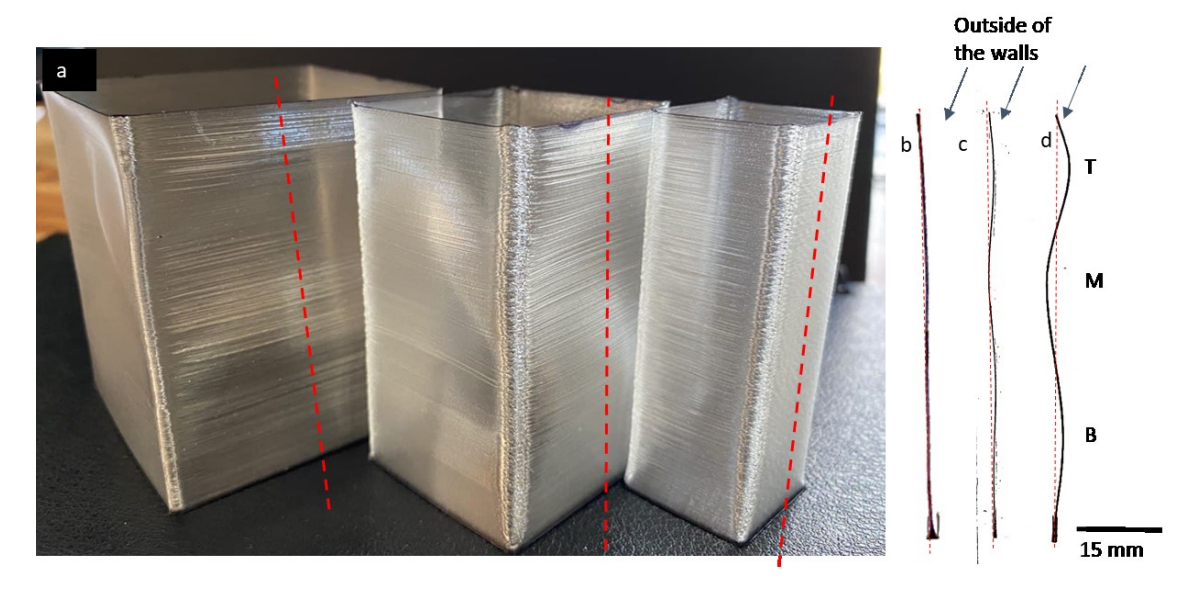


Figure 6. a. Printed boxes of Technomelt. Red dashed lines indicate the approximate locations at which cross-sections were imaged for warpage analysis. The imaged cross-sections of the box walls of length b. 25 mm; c. 40 mm; d. 60 mm. The black lines show warpage across real cross-sections and red dotted lines indicate the warp-free state of the walls. Warpage analysis was performed at the Top (T), Middle (M), and Bottom (B) of parts, where the warpage direction changes.

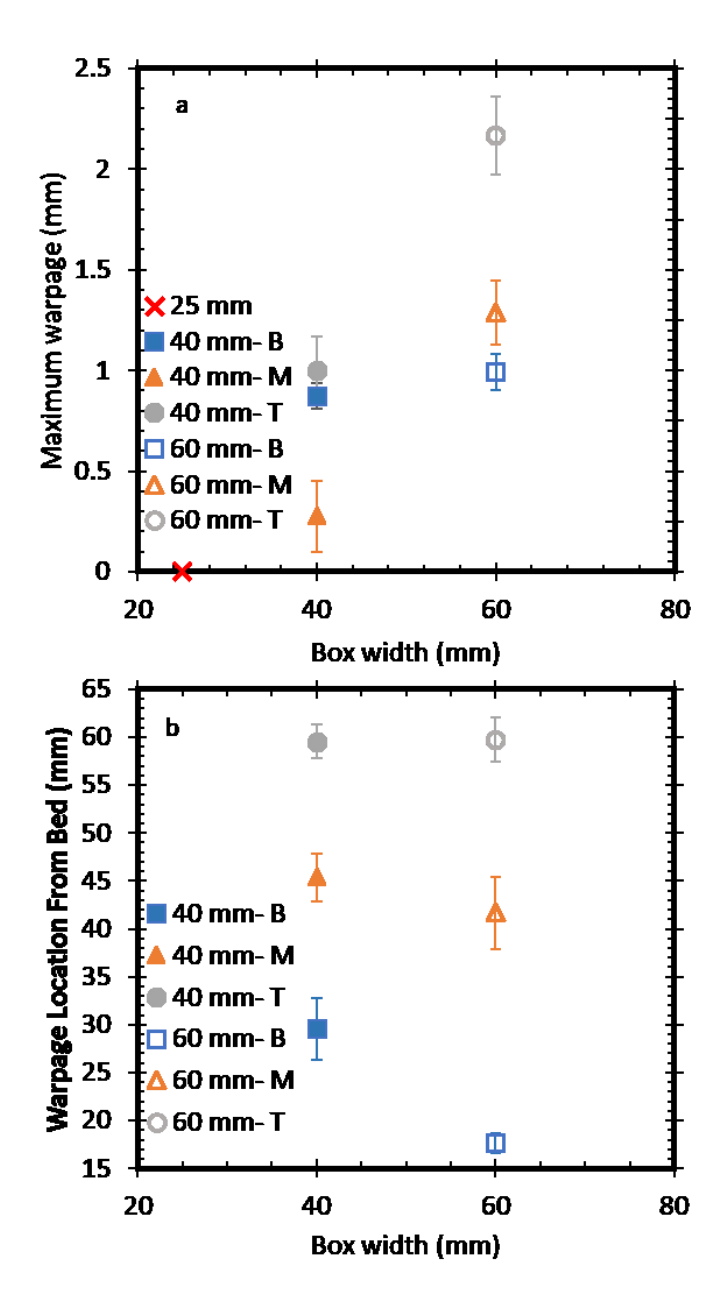


Figure 7. a. Average maximum warpage at the Top (T), Middle (M), and Bottom (B) of Technomelt boxes as measured from wall cross-sections; b. The location of the maximum warpage at T, B, and M as measured from the bottom of the boxes. The data represent the average value of measurements from walls of three different boxes, and error bars represent 95% confidence intervals.

Residual stresses contribute to tensile strength as well as warpage of printed structures.

As shown in Fig. 7, 25 mm boxes are free of warpage, while the 40 mm and 60 mm boxes show a

significant amount of warpage. The observed increase in warpage with increasing wall length is due to the larger thermomechanical stresses as a result of a larger temperature gradient between printed and newly deposited layers [27,46]. Increased warpage in thin parts with longer toolpaths is in agreement with the results from Xinhua et al. [47]. The warped regions result in stress concentration and can cause a drop in the tensile strength of parts.

Warpage is more severe in all three regions of 60 mm boxes compared to the 40 mm boxes. As shown in Fig. 7b, warpage at the top and middle of the 40 mm and 60 mm boxes occurs at approximately similar heights of 45 mm and 60 mm, respectively, while the bottom warpage happens at a lower height (17 mm) in the 60 mm box than in 40 mm boxes (30 mm). The difference in bottom warpage heights may be due to the different thermal histories in 40 mm and 60 mm boxes. Coogan et al. [34] reported higher environmental temperature close to the print bed, which resulted in increased strength of bottom layers and break of specimens at layers far from the build plate. The same reason might contribute to the warp-free bottom layers, and higher strength of bottom bars in 40 mm boxes. As shown in Fig. 1, bottom 90° bars are located at the height range of 5 mm to 30 mm from the bottom of boxes, which means that their gauge length is below the maximum warpage location (30 mm) in 40 mm boxes. This might be a reason for the higher tensile strength and tensile strain of bottom parts of 40 mm boxes compared to the top bars of 40 mm boxes in Fig. 3a. No warpage is observed in Loctite bars, which is related to the reinforcing effect of fibers. Glass fibers reduce the CTE of the composite, which results in lower shrinkage as the part cools from the printing temperature (240 °C) to ambient conditions [21].

3.4 OM and SEM

A wall cross-section for a 60 mm Loctite box is shown in Fig. 8. Glass fibers are highly oriented in the print direction, which contributes to the high yield strength of 0° specimens in Fig. 2b [29,48]. However, adhesion between the fibers and matrix is limited, as evidenced by the surfaces of debonded fibers, which are generally smooth with small traces of matrix material. This appearance is consistent with weak adhesion between the matrix and the fibers [29,49]. Poor adhesion between the matrix and fibers leads to ineffective stress transfer [50] and reduced mechanical properties.

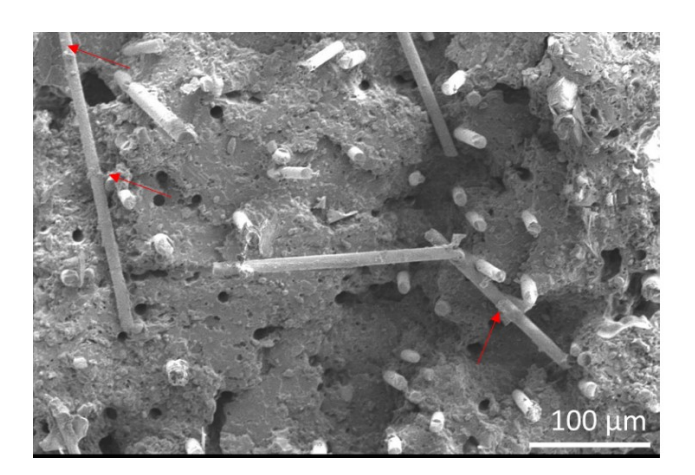


Figure 8. SEM of a wall cross-section from a 60 mm Loctite box.

Fracture surfaces of Loctite micro tensile bars with 0° and 90° raster angles are shown in Fig. 9. The smooth surface of 90° sample reveals brittle fracture of the specimen along the interlayer weld. The fracture surface of the 0° bar is rough, indicating ductile fracture that is consistent with the tensile properties in Fig. 3b and stress-strain curve in Fig. 4.

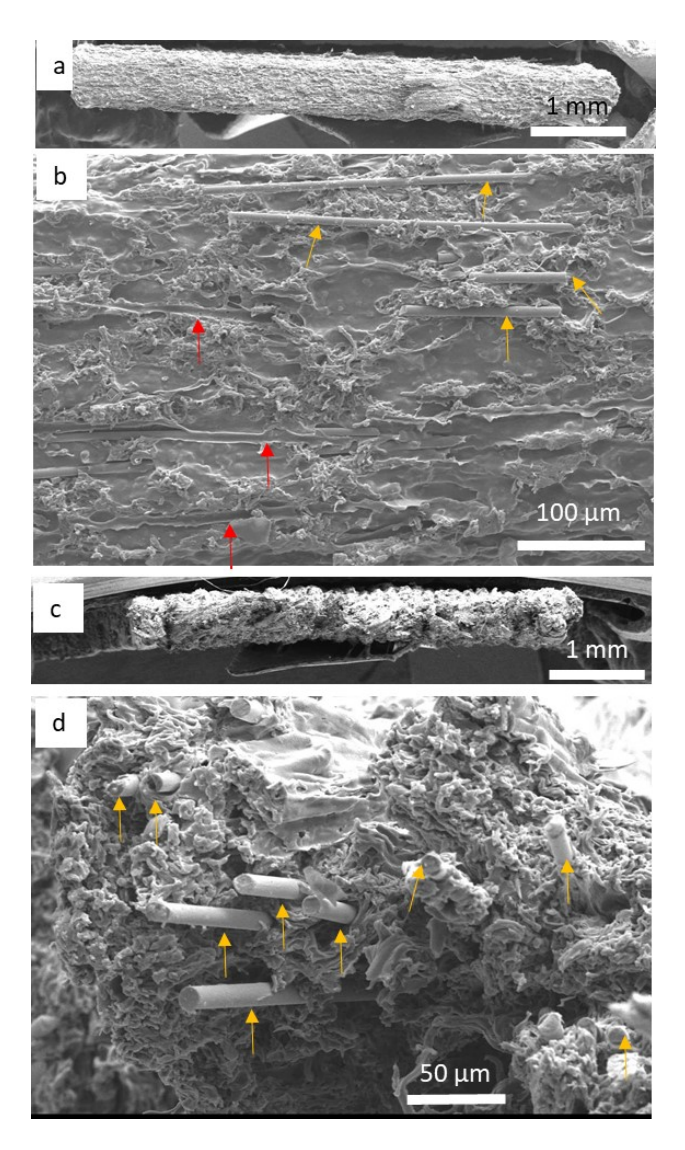


Figure 9. SEM images from fracture surfaces of micro tensile bars from 60 mm boxes: a. 90° raster angle; b. enlarged view of a; c. 0° raster angle; d. enlarged view of c. Yellow arrows highlight fibers and red arrows highlight the negative impression left by a fiber.

Freeze fractured cross-sections of the first few layers of Technomelt and Loctite boxes are shown in Fig. 10. Good coalescence between layers is observed in Technomelt, which contributes to the observed high weld strength. The coalescence between Loctite layers is worse than for Technomelt layers. Some voids with a similar dimensions to the fibers diameter are observed due to fiber pull-out during fracturing, and some larger voids can be seen as well, which are consistent with limited wetting and diffusion of polymer chains between layers. These voids act as stress

concentration areas and result in lower bond strength of layers, consistent with the low tensile strength of 90° samples in Fig. 3b.

The initial layers of Technomelt boxes exhibit slumping, with more significant slumping observed in 25 mm boxes, likely due to the shorter toolpath. Increasing the wall length at a constant printing speed results in longer cooling time before deposition of the next layer, which reduced layer spreading. In Loctite boxes, the effect of wall length on dimensional accuracy of prints is not significant because Loctite did not slump substantially under any investigated conditions.

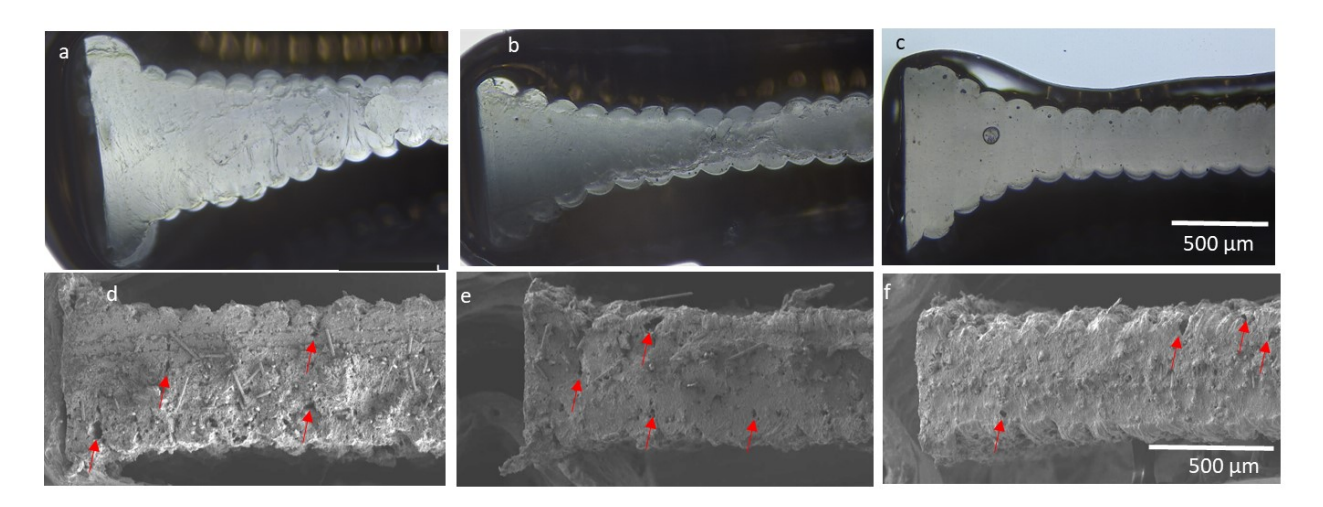


Figure 10. (a-c) Optical microscopy images from wall cross-sections of printed Technomelt boxes with the wall length of: a. 25 mm; b. 40 mm; c. 60 mm. (d-f) SEM images from wall cross-sections of printed Loctite boxes with the wall length of: a. 25 mm; b. 40 mm; c. 60 mm. The first deposited layer is located in the left side of each image, and the red arrows indicate the large voids on the Loctite cross-section.

The layer widths of the first layers of Technomelt and Loctite boxes as a function of wall length are plotted in Fig. 11. For 25 mm Technomelt boxes, the first layer without excessive spreading is layer 12, while it is layer 8 and layer 7 for the 40 mm and 60 mm boxes, respectively.

Loctite boxes could retain their shape starting at layer 3. The spread of the first layer increases by decreasing the wall length in Loctite boxes, while similar layer widths with a slight spread are observed in the second layer of all boxes. Limited slumping is observed in Loctite boxes, which is consistent with the presence of fibers and the increased viscosity they cause [51]. The layer width as a function of layer number for Technomelt and Loctite boxes is shown in Fig. SI6, which highlights the non-linear layer slumping. The achieved layer width without slumping for Technomelt is similar to the designed value of 0.4 mm. However, slightly larger layer widths are observed for Loctite boxes, which indicates consistent over-extrusion by the TAZ6.

Higher temperatures from shorter layer times lead to the observed increased slumping of boxes with decreased wall length in Fig. 10 and Fig. 11, which is consistent with the higher break strain and tensile strength of Technomelt boxes with a shorter wall length in Fig. 3a. The shorter wall length leads to less time for cooling and higher layer temperature, which facilitate reptation of polymer chains across the weld. Sun et al. reported 12 °C higher average building temperature in laterally built ABS parts with a shorter toolpath compared to the longitudinally built parts with a longer toolpath [52].

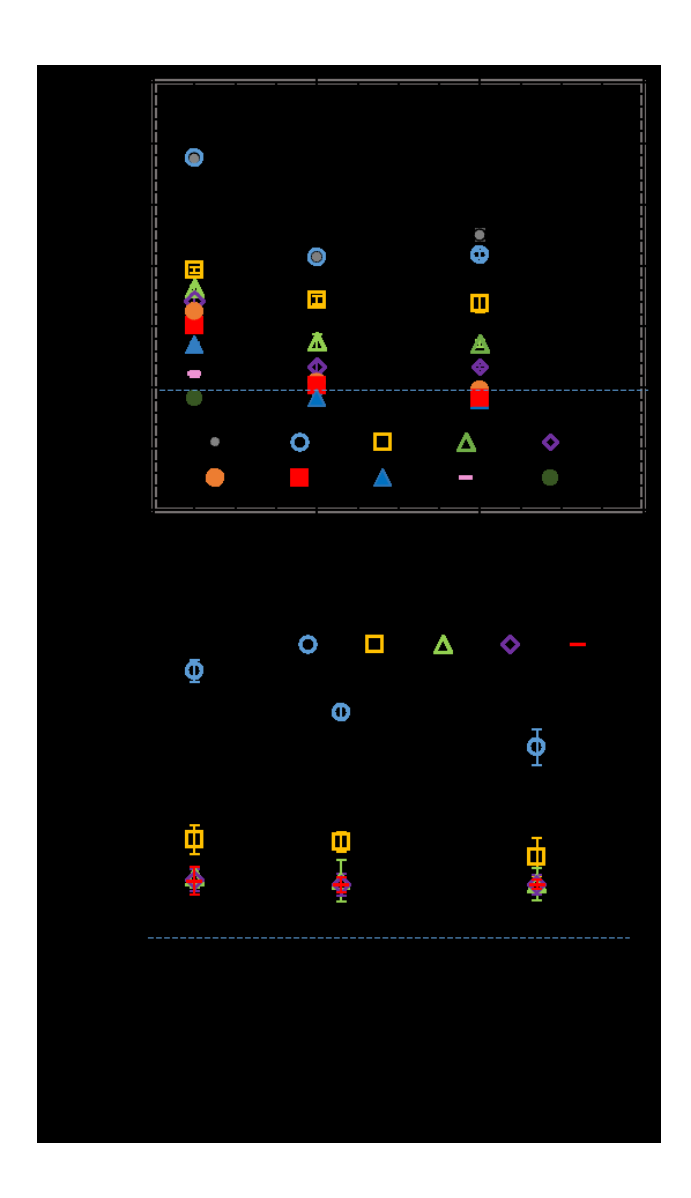


Figure 11. Layer width across different layers as a function of printed box wall length for: a. Technomelt; b. Loctite. Error bars represent 95% confidence intervals. Dotted lines represent the designed layer width.

3.5 Rheology

Results from capillary rheology of Technomelt and Loctite at different temperatures are shown in Fig. 12. Shear-thinning and a decrease in the viscosity with increasing temperature are observed for both materials, which are characteristic of thermoplastic materials. Bagley and Rabinowitch corrections were applied to the shear stress and shear rate data from capillary

rheology to account for entrance effects and a non-parabolic velocity profile. In comparing the viscosity of Loctite and Technomelt at their respective extrusion temperatures, Loctite has a higher viscosity in spite of a 20 °C higher extrusion temperature. Loctite's higher viscosity is due to the presence of glass fibers, which act as obstacles for polymer chain movements. The high viscosity prevents the slumping of initial layers, but the presence of glass fibers also reduces weld strength.

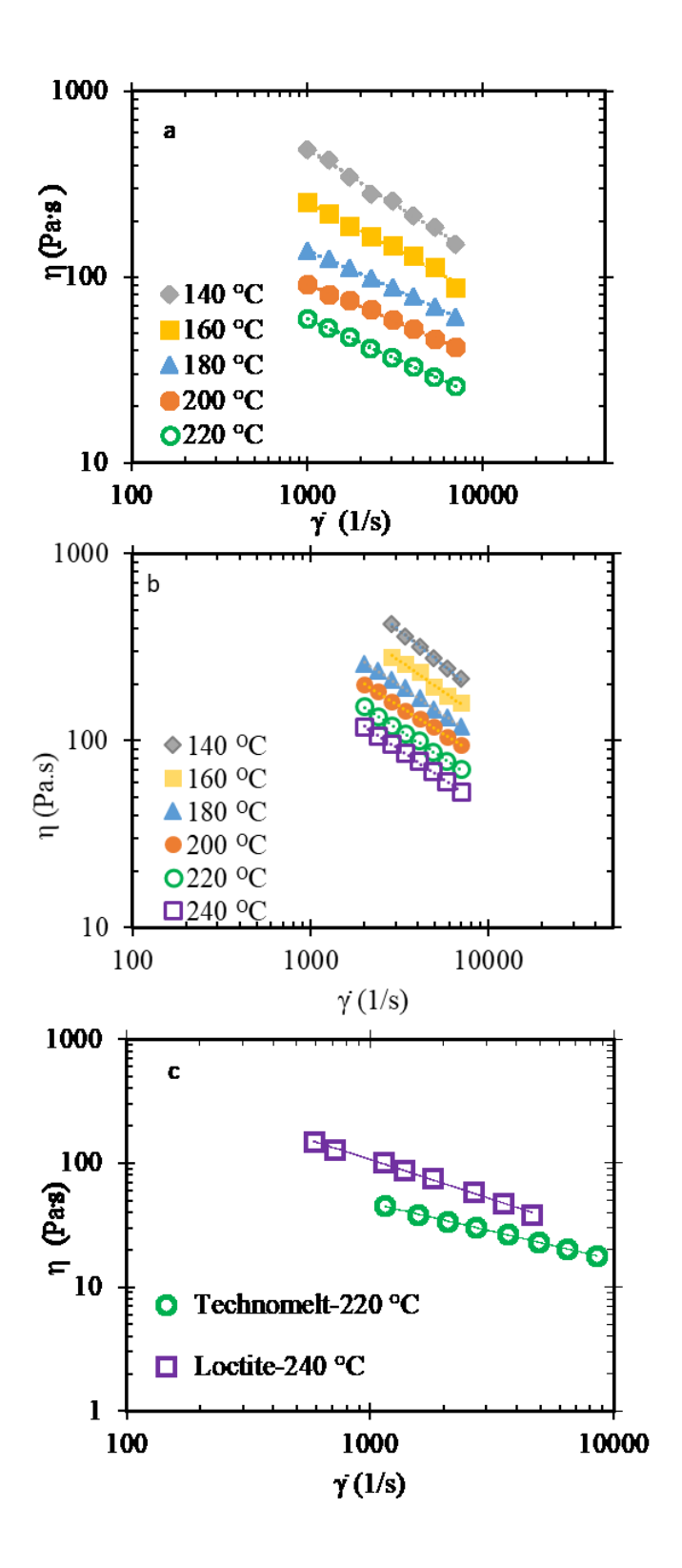


Figure 12. Capillary rheology of: a. Technomelt as-received pellets; b. Loctite as-received pellets at a range of FFF-relevant temperatures; c. Technomelt and Loctite at FFF extrusion temperatures.

3.6 Type V Tensile bars

To determine mechanical properties of Loctite prints that are more representative of the types of structures typically printed using FFF, ASTM D638 type V tensile bars were also printed. The results of tensile testing of type V bars are compared to the results from single wall boxes in Fig. 13. Since tensile properties of micro Loctite bars are independent from box size and location of bar on the box, micro bars are categorized based on their raster angle, and the average value of all specimens with a similar raster angle are considered as a single data point in Fig. 13. Type V Loctite bars are stronger, with significantly higher yield strength and tensile strength than single wall boxes. The yield strength and tensile strength of 90° type V Loctite bars are significantly higher than 90° micro bars, while a small difference is observed for 0° samples. More significant improvement in tensile properties of 90° bars compared to the 0° bars is related to the greater importance of weld strength in 90° samples, in which load is applied perpendicular to the weld line. A large number of fibers or fiber paths are observed at the weld interface of 90° micro Loctite bars in Fig. 9b. Fibers along the road surface affects the surface tension and decreases wettability between layers, which governs coalescence and welding between roads. Additionally, since polymer chains can't diffuse into fibers, these fibers act as obstacles for polymer diffusion and reduce interlayer welding [36].

The yield strength of type V Loctite bars is approximately 25% higher than Technomelt counterparts at a 0° raster angle, and slightly lower than Technomelt at a 90° raster angle in our previous study [32]. The observed increase in yield strength of Loctite is slightly below the usual range of 30-45% increase observed for FFF prints of fiber-reinforced thermoplastic composites

[53–55]. Gupta et al. [30] reported a 4% drop in yield strength of printed polycarbonate (PC) compounded with short carbon fibers due to the formation of local stresses produced by the imperfect alignment of short fibers. Large improvements in yield strength were reported by Tekinalp et al., whom showed a 115% increase in tensile strength of FFF prints of carbon fiber-reinforced ABS [29]. In another study, Abderrafai et al. increased the tensile strength of PA12 parts reinforced by carbon fibers by up to 115% [56]. Proper fiber-matrix selection accompanied by good adhesion between fibers and the matrix are important to achieving strong fiber-reinforced composites [57]. However, it should also be noted that FFF of Technomelt is capable of achieving void-free structures with tensile properties that are comparable to, or even better than, compression molded specimens. Therefore, the lower improvements in tensile strength may be due to the exceptional properties of the additively manufactured unreinforced polymer.

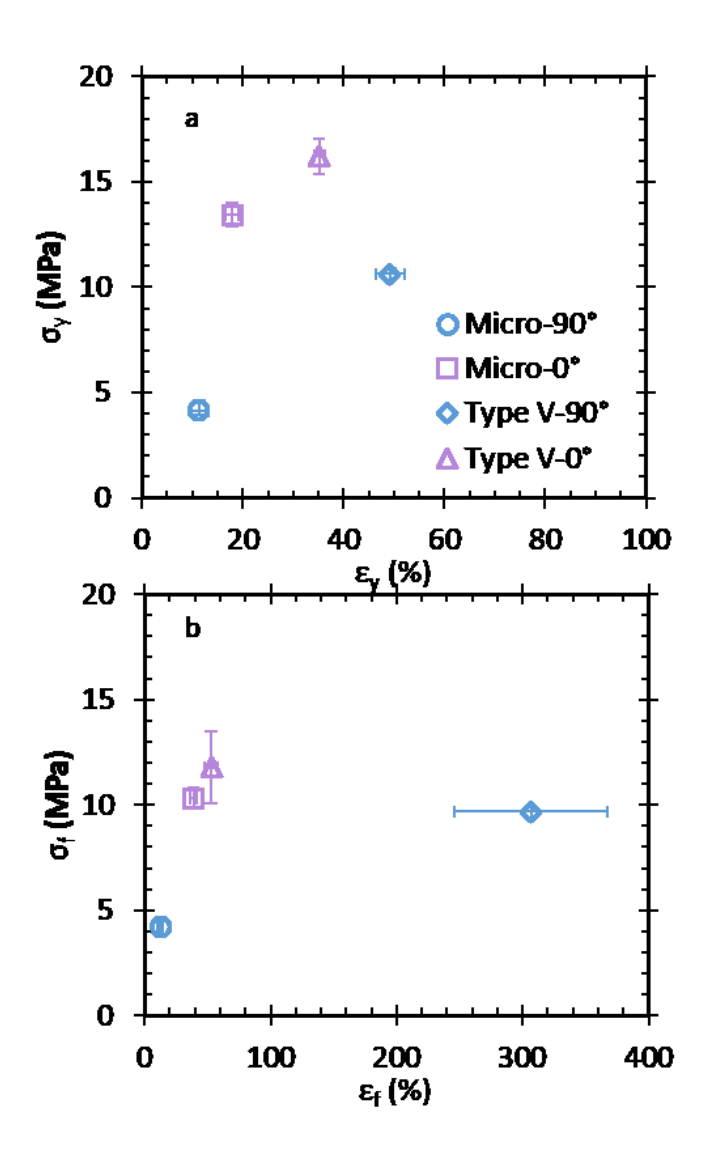


Figure 23. Tensile Properties of Loctite micro vs. type V Bars: a. Yield strength versus yield strain; b. Tensile strength versus strain to failure of micro and type V Loctite bars with the raster angles of 0°, and 90°. The results for micro Loctite bars are the average values from all specimens with a similar raster angle. Error bars represent 95% confidence intervals.

Fracture surfaces from tensile testing of Loctite bars with 0° and 90° raster angles are shown in Fig. 14. Both tensile bars exhibit a rough surface and plastic deformation before failure, which results in ductile fracture. The fractured surface of 90° tensile bar shows a significant reduction in cross-section area and severe deformation before failure, which is in accordance

with their representative stress-strain curves in Fig. SI7, and the larger break strain of 90° type V specimens in Fig. 13.

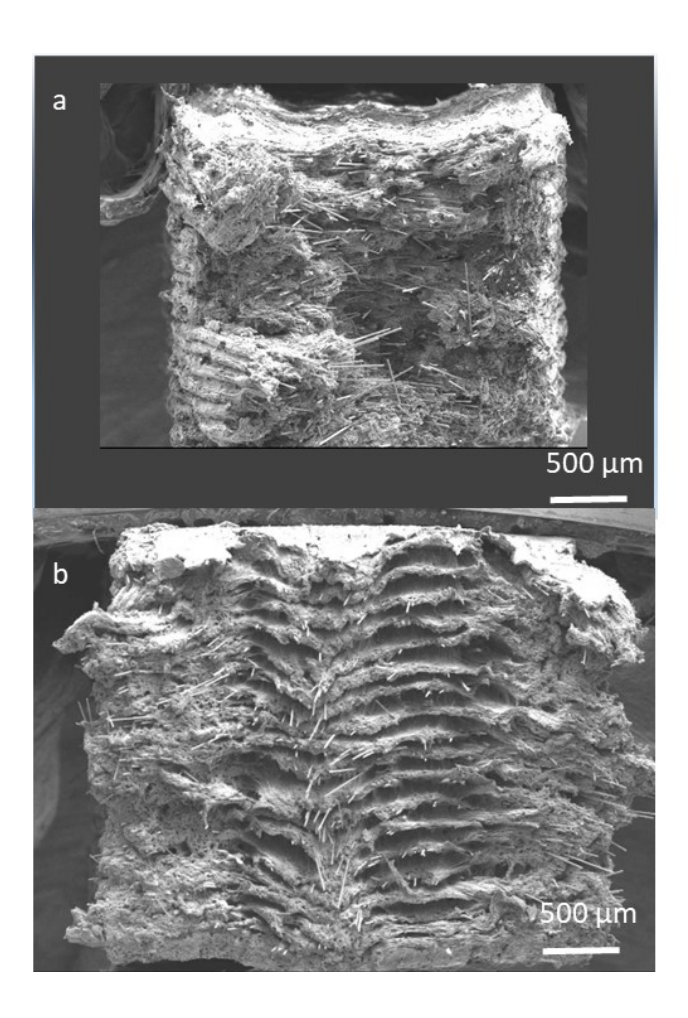


Figure 14. SEM images from tensile fractured cross-section of Type V Loctite tensile bars with raster angles of: a. 90°; b. 0°.

A freeze fractured cross-section of a 90° type V tensile bar is shown in Fig. 15. There is no obvious interface or FFF-related voids in the print interface, indicating good coalescence between layers due to a higher thermal mass in multilayer geometries, which contributes to the improvement in tensile properties of type V bars. The other potential reason for the significant increase in tensile properties of 90° type V bars compared to 90° micro bars is the different orientation of fibers in shell and infill region as is observed in the fractured cross-section due to

the different printing direction. In 90° type V bars, the infill is oriented perpendicular to the pulling direction and the shell is parallel to the pulling direction. In 0° samples, the shell and infill region are oriented parallel to the pulling direction as can be seen in Fig. 14b.

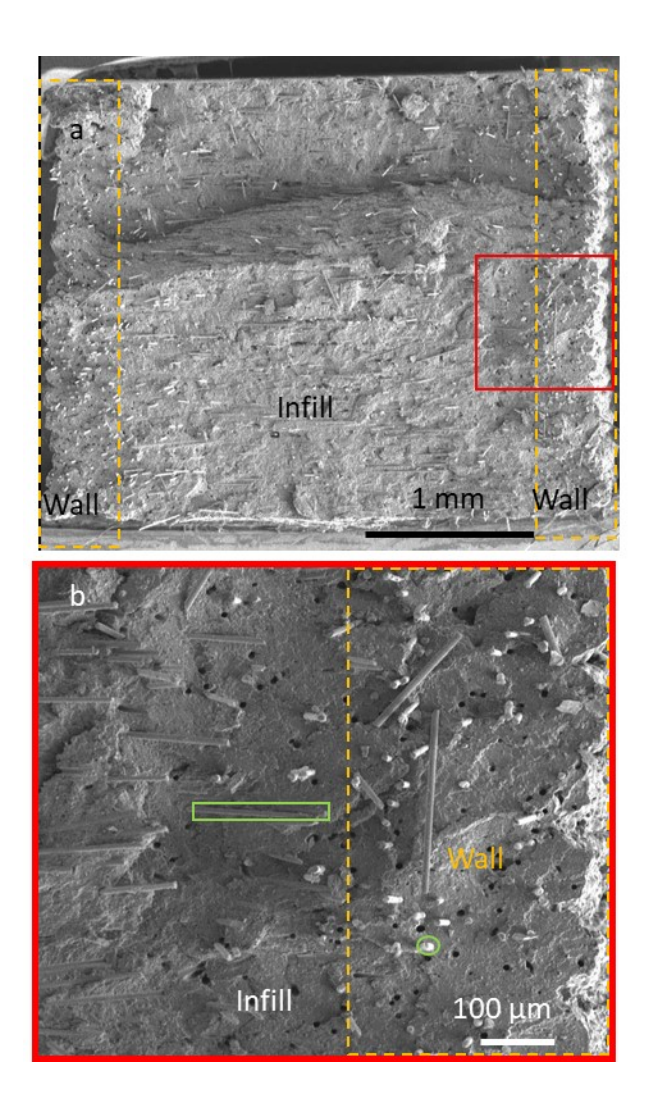


Figure. 15. a. SEM image from freeze fractured cross-section of Type V Loctite tensile bar with a raster angle of 90°; b. The enlarged view of the region within the red rectangle in Fig 15.a. The yellow dotted rectangles represent the wall of bars and green rectangle and circle indicate visible cross-section of fibers in the infill region and wall of the bar, respectively.

5. Conclusion

This paper aims to study the effect of glass fibers and toolpath on mechanical properties, warpage, and dimensional accuracy of print. Glass fibers in Loctite increase yield strength of 0° tensile bars, but decrease their elongation in this direction from hundreds of percent to about 50% which is still relatively quite high for a 3D resin. Fiber addition lead to incomplete wetting between rows in boxes, but not in the thicker Type V tensile bars, which are more representative of printed parts.

Warpage was only observed in Technomelt boxes, and it was more significant in boxes with a longer toolpath. Long toolpath induces longer cooling time for the layers, and results in large thermomechanical stresses and warpage of prints. The warpage and residual stresses cause early failure of parts. The presence of glass fibers prevented warpage in Loctite boxes. Glass fibers also prevented excessive spread of initial layers of boxes. The spread of layers was more significant in Technomelt boxes with shorter toolpaths, in which the layers could retain heat for a longer time before deposition of the next layer.

In summary, the addition of glass fibers results in substantial anisotropy for Loctite prints, which is much more significant in thin parts. Therefore, the toolpath needs to be optimized based on the application and load direction. However, glass fibers help with controlling warpage and maintaining dimensional accuracy of printed structures. Improved bond strength of multilayer Loctite bars compared to thin parts justifies their use in large structural applications, in which there is a high thermal mass and slumping is a concern.

Conflicts of interest

The authors declare that they have no known competing financial interests or personal relationships that could have appeared to influence the work reported in this paper

Acknowledgements

The authors acknowledge financial support from the National Science Foundation (CMMI-1853480). The authors also thank Henkel Corporation for providing Technomelt PA 6910 and Loctite 3D 6910 and thank Charles Paul, Luca Marchese, and Tim Welters of Henkel Corporation for insightful conversations and guidance.

References

- [1] S.H. Ahn, M. Montero, D. Odell, S. Roundy, P.K. Wright, Anisotropic material properties of fused deposition modeling ABS, Rapid Prototyping Journal. 4 (2002) 248–257. https://doi.org/10.1108/13552540210441166.
- [2] A.M. Peterson, Review of acrylonitrile butadiene styrene in fused filament fabrication: A plastics engineering-focused perspective, Additive Manufacturing. 27 (2019) 363–371. https://doi.org/10.1016/j.addma.2019.03.030.
- [3] C. Koch, L. van Hulle, N. Rudolph, Investigation of mechanical anisotropy of the fused filament fabrication process via customized tool path generation, Additive Manufacturing. 16 (2017) 138–145. https://doi.org/10.1016/j.addma.2017.06.003.
- [4] E.L. Gilmer, D. Miller, C.A. Chatham, C. Zawaski, J.J. Fallon, A. Pekkanen, T.E. Long, C.B. Williams, M.J. Bortner, Model analysis of feedstock behavior in fused filament fabrication: Enabling rapid materials screening, Polymer (Guildf). 152 (2018) 51–61. https://doi.org/10.1016/j.polymer.2017.11.068.
- [5] E.R. Fitzharris, D.W. Rosen, M.L. Shofner, Fast scanning calorimetry for semicrystalline polymers in fused deposition modeling, Polymer (Guildf). 166 (2019) 196–205. https://doi.org/10.1016/j.polymer.2019.01.083.
- [6] J.M. Gardner, C.J. Stelter, G. Sauti, J.W. Kim, E.A. Yashin, R.A. Wincheski, H.C. Schniepp, E.J. Siochi, Environment control in additive manufacturing of high-performance thermoplastics, International Journal of Advanced Manufacturing Technology. 119(9) (2022) 6423–6433. https://doi.org/10.1007/s00170-020-05538-w.

- [7] A. el Moumen, M. Tarfaoui, K. Lafdi, Modelling of the temperature and residual stress fields during 3D printing of polymer composites, International Journal of Advanced Manufacturing Technology. 104 (2019) 1661–1676. https://doi.org/10.1007/s00170-019-03965-y.
- [8] C.H. Lee, F.N.B.M. Padzil, S.H. Lee, Z.M.A. Ainun, L.C. Abdullah, Potential for natural fiber reinforcement in pla polymer filaments for fused deposition modeling (Fdm) additive manufacturing: A review, Polymers (Basel). 13(9) (2021) 1309–1407. https://doi.org/10.3390/polym13091407.
- [9] L. Benedetti, B. Brulé, N. Decreamer, K.E. Evans, O. Ghita, Shrinkage behaviour of semi-crystalline polymers in laser sintering: PEKK and PA12, Materials and Design. 181 (2019) 107906. https://doi.org/10.1016/j.matdes.2019.107906.
- [10] M. Abasalizadeh, R. Hasanzadeh, Z. Mohamadian, T. Azdast, M. Rostami, Experimental study to optimize shrinkage behavior of semi-crystalline and amorphous thermoplastics, Iranian Journal of Materials Science and Engineering. 15 (2018) 41–51. https://doi.org/10.22068/ijmse.15.4.41.
- [11] T.C. Chang, E. Faison III, Shrinkage Behavior and Optimization of Injection Molded Parts Studied by the Taguchi Method, Polymer Engineering & Science. 41(5) (2001) 703–710. https://doi.org/https://doi.org/10.1002/pen.10766.
- [12] A.A. Samy, A. Golbang, E. Harkin-Jones, E. Archer, M. Dahale, A. McIlhagger, Influence of Ambient Temperature on Part Distortion: A Simulation Study on Amorphous and Semi-Crystalline Polymer, Polymers (Basel). 14(5) (2022) 879. https://doi.org/10.3390/polym14050879.
- [13] E.R. Fitzharris, N. Watanabe, D.W. Rosen, M.L. Shofner, Effects of material properties on warpage in fused deposition modeling parts, International Journal of Advanced Manufacturing Technology. 95(5) (2018) 2059–2070. https://doi.org/10.1007/s00170-017-1340-8.
- [14] K. Rodzeń, E. Harkin-Jones, M. Wegrzyn, P.K. Sharma, A. Zhigunov, Improvement of the layer-layer adhesion in FFF 3D printed PEEK/carbon fibre composites, Composites Part A: Applied Science and Manufacturing. 149 (2021) 106532. https://doi.org/10.1016/j.compositesa.2021.106532.
- [15] T.M. Wang, J.T. Xi, Y. Jin, A model research for prototype warp deformation in the FDM process, International Journal of Advanced Manufacturing Technology. 33(11) (2007) 1087–1096. https://doi.org/10.1007/s00170-006-0556-9.
- [16] H. Prajapati, S.S. Salvi, D. Ravoori, M. Qasaimeh, A. Adnan, A. Jain, Improved print quality in fused filament fabrication through localized dispensing of hot air around the deposited filament, Additive Manufacturing. (2021). https://doi.org/10.1016/j.addma.2021.101917.
- [17] P. Han, S. Zhang, A. Tofangchi, K. Hsu, Relaxation of residual stress in fused filament fabrication part with in-process laser heating, Procedia Manufacturing. 53 (2021) 466–471. https://doi.org/10.1016/j.promfg.2021.06.080.
- [18] P. Han, A. Tofangchi, S. Zhang, A. Desphande, K. Hsu, Effect of in-process laser interface heating on strength isotropy of extrusion-based additively manufactured PEEK, Procedia Manufacturing. 48 (2020) 737–742. https://doi.org/10.1016/j.promfg.2020.05.107.

- [19] A. Dey, I.N.R. Eagle, N. Yodo, A review on filament materials for fused filament fabrication, Journal of Manufacturing and Materials Processing. 5(3) (2021) 69. https://doi.org/10.3390/jmmp5030069.
- [20] S. Dul, L. Fambri, A. Pegoretti, Fused deposition modelling with ABS-graphene nanocomposites, Composites Part A: Applied Science and Manufacturing. 85 (2016) 181–191. https://doi.org/10.1016/j.compositesa.2016.03.013.
- [21] L.J. Love, V. Kunc, O. Rios, C.E. Duty, A.M. Elliott, B.K. Post, R.J. Smith, C.A. Blue, The importance of carbon fiber to polymer additive manufacturing, Journal of Materials Research. 29(17) (2014) 1893–1898. https://doi.org/10.1557/jmr.2014.212.
- [22] C.G. Schirmeister, T. Hees, E.H. Licht, R. Mülhaupt, 3D printing of high density polyethylene by fused filament fabrication, Additive Manufacturing. 28 (2019) 152–159. https://doi.org/10.1016/j.addma.2019.05.003.
- [23] G. Ćwikła, C. Grabowik, K. Kalinowski, I. Paprocka, P. Ociepka, The influence of printing parameters on selected mechanical properties of FDM/FFF 3D-printed parts, IOP Conference Series: Materials Science and Engineering. 227 (2017) 012033. https://doi.org/10.1088/1757-899X/227/1/012033.
- [24] Y.-H. Choi, C.-M. Kim, H.-S. Jeong, J.-H. Youn, Influence of Bed Temperature on Heat Shrinkage Shape Error in FDM Additive Manufacturing of the ABS-Engineering Plastic, World Journal of Engineering and Technology. 4(3) (2016) 186–192. https://doi.org/10.4236/wjet.2016.43d022.
- [25] M. Jin, C. Neuber, H.W. Schmidt, Tailoring polypropylene for extrusion-based additive manufacturing, Additive Manufacturing. 33 (2020) 101101. https://doi.org/10.1016/j.addma.2020.101101.
- [26] M. Spoerk, C. Savandaiah, F. Arbeiter, G. Traxler, L. Cardon, C. Holzer, J. Sapkota, Anisotropic properties of oriented short carbon fibre filled polypropylene parts fabricated by extrusion-based additive manufacturing, Composites Part A: Applied Science and Manufacturing. 113 (2018) 95–104. https://doi.org/10.1016/j.compositesa.2018.06.018.
- [27] G. Sodeifian, S. Ghaseminejad, A.A. Yousefi, Preparation of polypropylene/short glass fiber composite as Fused Deposition Modeling (FDM) filament, Results in Physics. 12 (2019) 205–222. https://doi.org/10.1016/j.rinp.2018.11.065.
- [28] O.S. Carneiro, A.F. Silva, R. Gomes, Fused deposition modeling with polypropylene, Materials & Design. 83 (2015) 768–776. https://doi.org/10.1016/j.matdes.2015.06.053.
- [29] H.L. Tekinalp, V. Kunc, G.M. Velez-Garcia, C.E. Duty, L.J. Love, A.K. Naskar, C.A. Blue, S. Ozcan, Highly oriented carbon fiber-polymer composites via additive manufacturing, Composites Science and Technology. 105 (2014) 144–150. https://doi.org/10.1016/j.compscitech.2014.10.009.
- [30] A. Gupta, I. Fidan, S. Hasanov, A. Nasirov, Processing, mechanical characterization, and micrography of 3D-printed short carbon fiber reinforced polycarbonate polymer matrix composite material, International Journal of Advanced Manufacturing Technology. 107(7) (2020) 3185–3205. https://doi.org/10.1007/s00170-020-05195-z.

- [31] G.D. Goh, Y.L. Yap, S. Agarwala, W.Y. Yeong, Recent Progress in Additive Manufacturing of Fiber Reinforced Polymer Composite, Advanced Materials Technologies. 4(1) (2019) 1800271. https://doi.org/10.1002/admt.201800271.
- [32] M. Pourali, A.M. Peterson, Fused filament fabrication of void-free parts using low viscosity hot melt adhesives, Additive Manufacturing. 46 (2021) 102110. https://doi.org/10.1016/j.addma.2021.102110.
- [33] DUS Architects, 3D Print Canal House, (2014) 230.
- [34] T.J. Coogan, D.O. Kazmer, Bond and part strength in fused deposition modeling, Rapid Prototyping Journal. 23 (2017) 414–422. https://doi.org/10.1108/RPJ-03-2016-0050.
- [35] C. Bellehumeur, L. Li, Q. Sun, P. Gu, Modeling of bond formation between polymer filaments in the fused deposition modeling process, Journal of Manufacturing Processes. 6(2) (2004) 170–178. https://doi.org/10.1016/S1526-6125(04)70071-7.
- [36] B. Brenken, E. Barocio, A. Favaloro, V. Kunc, R.B. Pipes, Fused filament fabrication of fiber-reinforced polymers: A review, Additive Manufacturing. 21 (2018) 1–16. https://doi.org/10.1016/j.addma.2018.01.002.
- [37] S.Y. Fu, B. Lauke, E. Mäder, C.Y. Yue, X. Hu, Tensile properties of short-glass-fiber- and short-carbon-fiber-reinforced polypropylene composites, Composites Part A: Applied Science and Manufacturing. 31(10) (2000) 1117–1125. https://doi.org/10.1016/S1359-835X(00)00068-3.
- [38] H.G.H. van Melick, L.E. Govaert, H.E.H. Meijer, On the origin of strain hardening in glassy polymers, Polymer (Guildf). 44(8) (2003) 2493–2502. https://doi.org/10.1016/S0032-3861(03)00112-5.
- [39] R.P. Wool, K.M. O'Connor, A theory of crack healing in polymers, Journal of Applied Physics. 52(10) (1981) 5953–5963. https://doi.org/10.1063/1.328526.
- [40] R.P. Wool, K.M. O'Connor, Time dependence of crack healing., Journal of Polymer Science. Part B, Polymer Letters. 20(1) (1982) 7–16. https://doi.org/10.1002/pol.1982.130200102.
- [41] E. Barocio, B. Brenken, A. Favaloro, R.B. Pipes, Interlayer fusion bonding of semi-crystalline polymer composites in extrusion deposition additive manufacturing, Composites Science and Technology. (2022) 109334. https://doi.org/10.1016/j.compscitech.2022.109334.
- [42] G.D. Smith, C.J.G. Plummer, P.E. Bourban, J.A.E. Månson, Non-isothermal fusion bonding of polypropylene, Polymer (Guildf). 42 (2001) 6247–6257. https://doi.org/10.1016/S0032-3861(01)00060-X.
- [43] C.J.G. Plummer, P.E. Bourban, J.E. Zanetto, G.D. Smith, J.A.E. Månson, Nonisothermal fusion bonding in semicrystalline thermoplastics, Journal of Applied Polymer Science. 87(8) (2002) 1267–1276. https://doi.org/10.1002/app.11528.
- [44] M. Pourali, A.M. Peterson, A tale of two polyamides: comparing the crystallization kinetics of a hot-melt adhesive and a PA 6/66 copolymer, Thermochimica Acta. 710 (2022) 179176. https://doi.org/10.1016/j.tca.2022.179176.

- [45] W. Yu, X. Wang, E. Ferraris, J. Zhang, Melt crystallization of PLA/Talc in fused filament fabrication, Materials and Design. 182 (2019) 108013. https://doi.org/10.1016/j.matdes.2019.108013.
- [46] A. Armillotta, M. Bellotti, M. Cavallaro, Warpage of FDM parts: Experimental tests and analytic model, Robotics and Computer-Integrated Manufacturing. 50 (2018) 140–152. https://doi.org/10.1016/j.rcim.2017.09.007.
- [47] L. Xinhua, L. Shengpeng, L. Zhou, Z. Xianhua, C. Xiaohu, W. Zhongbin, An investigation on distortion of PLA thin-plate part in the FDM process, International Journal of Advanced Manufacturing Technology. 79(5) (2015) 1117–1126. https://doi.org/10.1007/s00170-015-6893-9.
- [48] E. Shulga, R. Karamov, I.S. Sergeichev, S.D. Konev, L.I. Shurygina, I.S. Akhatov, S.D. Shandakov, A.G. Nasibulin, Fused filament fabricated polypropylene composite reinforced by aligned glass fibers, Materials. 13(16) (2020) 3442. https://doi.org/10.3390/MA13163442.
- [49] N. Gamze Karsli, T. Yilmaz, A. Aytac, G. Ozkoc, Investigation of erosive wear behavior and physical properties of SGF and/or calcite reinforced ABS/PA6 composites, Composites Part B: Engineering. 44(1) (2013) 385–393. https://doi.org/10.1016/j.compositesb.2012.04.074.
- [50] L.G. Tang, J.L. Karoos, A review of methods for improving the interfacial adhesion between carbon fiber and polymer matrix, Polymer Composites. 18(1) (1997) 100–113. https://doi.org/10.1002/pc.10265.
- [51] R. Petrucci, L. Torre, Filled Polymer Composites, in: Modification of Polymer Properties, 2017: pp. 23–46. https://doi.org/10.1016/B978-0-323-44353-1.00002-6.
- [52] Q. Sun, G.M. Rizvi, C.T. Bellehumeur, P. Gu, Effect of processing conditions on the bonding quality of FDM polymer filaments, Rapid Prototyping Journal. 14 (2008) 72–80. https://doi.org/10.1108/13552540810862028.
- [53] W. Zhang, C. Cotton, J. Sun, D. Heider, B. Gu, B. Sun, T.W. Chou, Interfacial bonding strength of short carbon fiber/acrylonitrile-butadiene-styrene composites fabricated by fused deposition modeling, Composites Part B: Engineering. 137 (2018) 51–59. https://doi.org/10.1016/j.compositesb.2017.11.018.
- [54] L. Sang, S. Han, Z. Li, X. Yang, W. Hou, Development of short basalt fiber reinforced polylactide composites and their feasible evaluation for 3D printing applications, Composites Part B: Engineering. 164 (2019) 629–639. https://doi.org/10.1016/j.compositesb.2019.01.085.
- [55] F. Ning, W. Cong, J. Qiu, J. Wei, S. Wang, Additive manufacturing of carbon fiber reinforced thermoplastic composites using fused deposition modeling, Composites Part B: Engineering. 80 (2015) 369–378. https://doi.org/10.1016/j.compositesb.2015.06.013.
- [56] Y. Abderrafai, M. Hadi Mahdavi, F. Sosa-Rey, C. Hérard, I. Otero Navas, N. Piccirelli, M. Lévesque, D. Therriault, Additive manufacturing of short carbon fiber-reinforced polyamide composites by fused filament fabrication: Formulation, manufacturing and characterization, Materials and Design. 214 (2022) 110358. https://doi.org/10.1016/j.matdes.2021.110358.

[57] J. Pratama, S.I. Cahyono, S. Suyitno, M.A. Muflikhun, U.A. Salim, M. Mahardika, B. Arifvianto, A review on reinforcement methods for polymeric materials processed using fused filament fabrication (FFF), Polymers (Basel). 13(22) (2021) 4022. https://doi.org/10.3390/polym13224022.